Failure Mechanisms and Rehabilitation Scenarios for Concrete Hydroelectric Facilities Affected by Alkali–Aggregate Reaction

Mahdi Ben Ftima[1*] and Emre Yildiz[2]

Abstract

This work focuses on the failure mechanisms of concrete hydroelectric facilities affected by alkali–aggregate reaction (AAR). Identification of potential failure mechanisms is based on an original "top-down approach" using an AAR pushover analysis with multi-physics numerical simulation of a representative hydroelectric facility. Different global rehabilitation scenarios based on slot-cutting and grouting techniques are discussed and compared, using different performance metrics. A new quantitative performance metric, specifically developed for the nonlinear sophisticated analysis tool and considering the volumetric cracking caused by AAR is also suggested. Based on comparison results, a combination of grouting after a partial slot-cutting in the neighborhood of the discontinuities, appears to provide the best compromise in terms of stress relief and extent of cracking. New AAR benchmark problems, issued from the top-down approach, are also suggested for the first time in the literature.

Keywords Alkali–aggregate reaction, Concrete hydroelectric facilities, Failure mechanism, Retrofitting strategies, Multi-physical simulation, Nonlinear finite element analysis

1 Introduction

Alkali–aggregate reaction (AAR) is an acid–base chemical reaction known to occur in concrete for certain types of aggregates and under certain moisture, confinement and temperature conditions. Swelling occurs due to the expansive nature of the alkali-silica gel, product of this reaction, when it comes in contact with moisture. This internal expansion generally leads to micro-cracking, loss of strength and stiffness at the *material scale.* Distortions can occur at the *structural* scale leading to functional problems of the equipment. At a higher *facility scale*, large structures may interact with each other, leading to macro-cracking in the cases of abrupt changes in stiffness or in geometrical configuration. Fig. 1 presents an example of a hydroelectric facility affected by AAR, where stiffness discontinuity between the right bank gravity dam and spillway, caused an inclined crack at the spillway pier/gravity dam corner. Several hydroelectric facilities around the world have been subjected to deteriorations induced by AAR, impairing their durability and serviceability. Typical examples have been reported in the literature such as Mactaquac, Canada (Gocevski and Yildiz 2017), Fontana dam, USA (Comi et al., 2009), and Temple-sur-Lot spillway piers, France (Sellier et al., 2009).

Most of the reported problems in the literature are related to functionality issues (Léger et al., 1995): discrete cracking, water seepage, ovalization distortions of the spiral/semi-spiral case rings, misalignments problems in superstructure, joint openings, gate jamming, etc. Only few references were interested in the ultimate condition or structural safety issues of the facility (e.g., Ben Ftima et al., 2017; FERC, 2018; USBR, 2005; Vulliet et al., 2017). The main reason behind this fact is believed to be the

*Correspondence:
Mahdi Ben Ftima
mahdi.ben-ftima@polymtl.ca
[1] École Polytechnique de Montréal, Montreal, Canada
[2] IDAE Inc., Montreal, Canada

Fig. 1 Hydroelectric facility affected by AAR: **a** facility overview; **b** formation of a concrete wedge (modified from Vulliet et al., 2017)

deformational nature of AAR expansion. As opposed to load-driven effects (e.g., mechanical loadings, hydrostatic pressure, etc.), displacement-driven effects (e.g., temperature, AAR, shrinkage, etc.) are known to be less severe with regard to failure and ultimate state condition. Nevertheless, the combination of these two different effects can be critical. The example in Fig. 1.b shows a simultaneous application of AAR induced thrust and hydrostatic loading on the spillway pier. This simultaneous application of displacement and force-driven effects is very common in the hydraulic structures field and constitutes the first motivation behind this work. The second motivation lies in the recent developments of computational frameworks which have made possible numerical simulation of AAR for large models at the facility scale (Ben Ftima et al., 2017, 2020).

This paper focuses on the failure mechanisms of hydroelectric facilities affected by AAR. Identification of *potential failure mechanisms* (PFM) is based on an original "top-down approach" using an *AAR pushover* multi-physics numerical analysis of a representative hydroelectric facility. By analogy with the pushover analysis in earthquake engineering using seismic excitation, a pushover analysis is carried out in this study by gradually increasing the deformations induced by AAR. Different conventional and new corrective actions are discussed and compared, using existing and new developed performance metrics/indicators. New benchmark problems issued from the top-down approach are also suggested for the first time in the literature.

2 Approach and Computational Framework
### 2.1 Approach Philosophy
Finite element (FE) models were commonly used in close conjunction with field monitoring as a continuous structural health monitoring (SHM) tool to predict the displacement field of some critical components of the facilities (Fig. 2a). A typical example is the prediction of lateral displacement of spillway gates of an AAR affected structure, to assist in the structural evaluation of gate jamming problem. Monitoring of vertical displacement of points on the crest of dams is generally used to calibrate the kinetics of the AAR model used in the FE simulations. A linear kinetics model with constant expansion rate has been commonly used in engineering and found to be adequate due to the relatively narrow width of the monitoring timeframe ($[t_1, t_n]$ in Figs. 2a and c) with respect to AAR kinetics (hundreds of years). It is however known that linear kinetics are not representative of the true chemical behavior at the material level (Larive, 1998). Bi-linear or nonlinear kinetics can be used instead, leading to more unknowns to be identified using monitoring data. As an example, Larive model is shown in Fig. 2c, where kinetics are expressed in terms of AAR advancement scalar $\xi(t)$ ($\xi = 0$ at the beginning of AAR reaction and 1.0 at the end of reaction). According to this model:

$$\xi(t) = \frac{1 - e^{\frac{t}{\tau_c}}}{1 + e^{-\frac{t-\tau_l}{\tau_c}}}, \tag{1}$$

where τ_l and τ_c are, respectively, the latency and characteristic times that depend on local temperature, stress and moisture conditions. Parameters τ_l and τ_c are the two unknowns that can be identified through monitoring and/or AAR accelerated laboratory tests for reference temperature and moisture condition (e.g., Sellier et al., 2009).

Unlike continuous SHM, the residual strength and stability assessment is a '*snapshot*' estimation of the safety of the structure or a substructure for an identified critical future time t_{n+1} and an identified potential failure
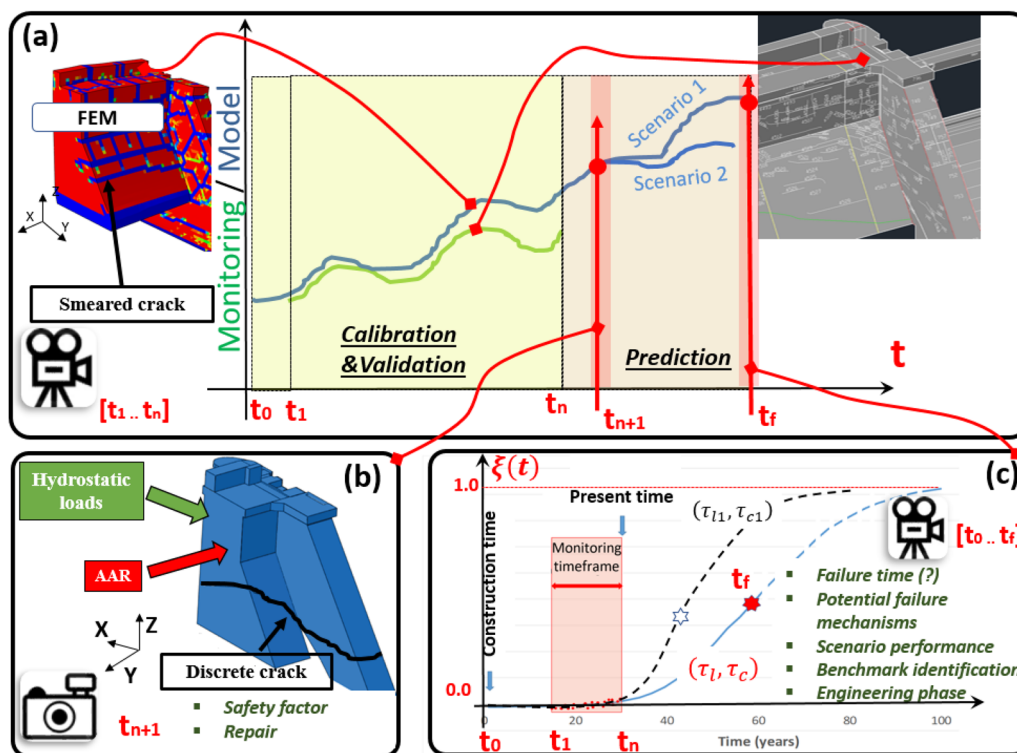
Fig. 2 AAR approaches: **a** continuous structural health monitoring approach (modified from Ben Ftima et al., 2017); **b** engineering approach; **c** suggested pushover approach

mechanism (Ben Ftima et al., 2017). For the example shown in Fig. 2a, b, 3D potential failure surface was identified by site investigations and raised the stability problem of an upper wedge concrete block. The assessment of safety factors and evaluation of potential major rehabilitation scenarios is then required in this phase and can be viewed as the "*true*" engineering phase.

The assessment of failure time t_f using nonlinear FE is a challenging task for the available concrete constitutive models (Fig. 2c). It shall be based on 3D finite element models using appropriate multi-physics concrete representation. Numerous models were suggested in the literature to simulate the complex AAR phenomenon and the effect of interventions. Of course, not all the developed approaches are feasible in the context of simulation of large numerical models (overall facility) over several years (say 100 years). Among the models named macro-models, the coupled chemo-mechanical models are of particular interest because they explicitly account for the kinetics of the chemical reaction depending on environmental conditions (mainly temperature and moisture conditions) and consider the anisotropy of swelling depending on the stress state (e.g., Léger et al., 1996; Omikrine et al., 2014; Saouma & Perotti, 2006; Sellier et al., 2009). According to the authors opinion, accurate

prediction of the failure time is very difficult and constitutes an on-going R&D field. The creation of the RILEM technical committee Internal Swelling Reaction (RILEM TC 259-ISR (2019)) in the year 2014 is a fact in favor of this finding. Three main reasons are behind this fact: (i) little or no validation experiments (Benchmarks) at a higher facility level, for the few available macro chemo-mechanical constitutive models; (ii) uncertainties in the assessment of kinetics of AAR; (iii) lack of consensus on deterioration kinetics of concrete material properties such as tensile strength and fracture energy and difficulty in assessing model input parameters for an existing facility.

Rather than focusing on the kinetics of AAR and the failure time, this work focuses on the identification of potential failure mechanisms (PFMs) using *a representative typical hydroelectric facility*. An "*AAR pushover analysis*" is performed on this facility, in terms of the AAR advancement field ξ (Fig. 2c). All mechanical loads (gravity and hydrostatic loads = load-driven effects) are applied in the first year. Deformation-driven and time-dependent effects are then applied continuously: creep effects, seasonal temperature effects and increasing AAR effects (ξ from 0.0 to 1.0). It is important to consider a chemo-mechanical constitutive model in this AAR

pushover analysis, to capture swelling gradient effects that have important influence on failure mechanisms as it will be shown later. Hence, at each time increment, the AAR advancement field is updated at each material point, depending on local temperature, T, and relative humidity, H, conditions ($\xi = \xi(x, y, z, T, H, t)$). Because Larive model is used in this study, this dependency is implicitly considered as described earlier in Eq. 1. A chemomechanical model developed in previous study (Ben Ftima et al., 2020), considering three sequentially coupled thermal, hygral and multi-physical FE analyses is used in this work. As shown in Fig. 2c, four important outcomes are anticipated from this original AAR pushover analysis: (1) identification of potential failure mechanisms; (2) performance comparisons of different corrective actions; (3) development of relevant benchmark problems for verification and validation (V&V) of computational framework, and (4) engineering phase on identified failure mechanisms.

Identification of benchmarks is based on a top-down approach as required by modern V&V recommendations (Oberkampf & Roy, 2010). As shown in Fig. 3.a, conventional V&V experiments were developed following a "*bottom-up*" approach starting with unit testing at the material level, then progressing towards structural components and the complete system (e.g., RILEM TC 259-ISR). Following the "*top-down approach*" considered in this study, the AAR pushover analysis of the representative hydroelectric facility at the top of the pyramid was performed to identify PFMs. Relevant *benchmark problems* (BPs) to verify the capability of AAR models to characterize these PFMs can therefore be developed. As

it will be shown, BPs at higher levels (e.g., level of group of elements in Fig. 3a) can be developed using this original approach.
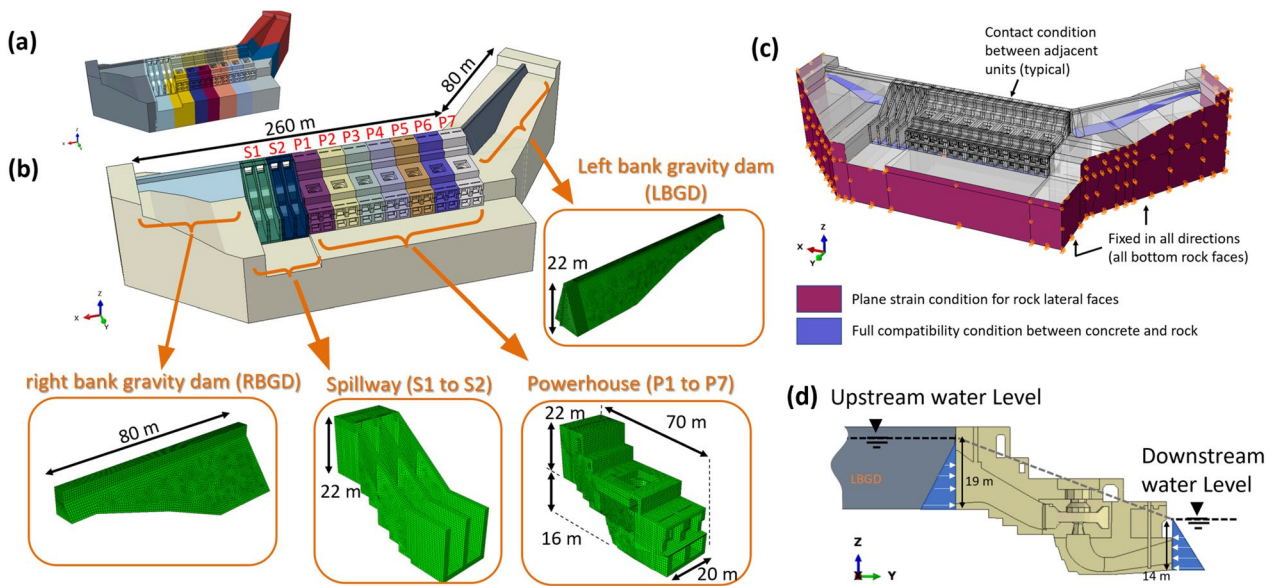
2.2 Representative Facility

A typical hydroelectric facility, representative of existing AAR affected facilities in North America, was designed to identify as many potential failure mechanisms as possible. The choice was made on a run-of-river facility including all types of components: dam, spillway and powerhouse (Fig. 4). As discontinuity is known to be the most important source for AAR structural manifestation, two types of discontinuities were included in the facility: stiffness discontinuity and geometrical discontinuity. The stiffness discontinuity was in the longitudinal axis of the powerhouse units occurring at P1/S2 and S1/RBGD intersections (Fig. 4b); and the geometrical discontinuity due to the angle between the longitudinal axis of the powerhouse units and the longitudinal axis of LBGD.

Mesh refinement is shown for the typical components in Fig. 4b. The model has more than 2.0 million degrees-of-freedom. The parallel processing ability was used, the FE model is therefore subdivided into fourteen domains, and each domain is represented with a separate color as shown in Fig. 4a. The hydraulic passage in the semi-spiral case was simplified to avoid mesh distortions. Also, by hypothesis, no reinforcement was considered in the model, except for the spillways where a conventional 25 M@300 rebar reinforcement was included in each direction. Though the mesh appears to be very refined, it is not refined enough to capture local and brittle failures
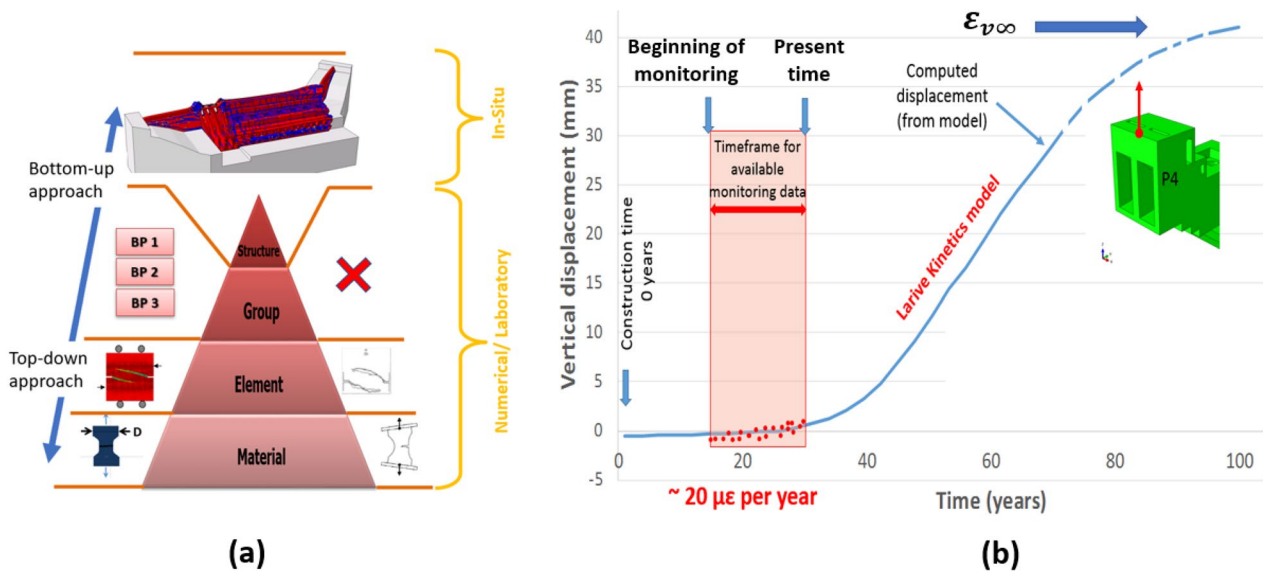
Fig. 3 V&V approaches: **a** bottom-up and top-down approaches; **b** calibration of AAR kinetic input parameters

Fig. 4 Geometry of the representative facility and mechanical boundary conditions: **a** domain decomposition; **b** geometry and mesh of typical components; **c** boundary conditions; **d** applied hydrostatic loads

as it will be shown in "Local analysis of spillway bridge" section, and sub-structuring is therefore required.

2.3 Computational Framework

The computational framework used in this work is a multi-physics framework developed by Ben Ftima et al., 2020. It uses three different finite element analyses with a *sequential coupling* (staggered analysis), as shown in Fig. 5a. In a first step, implicit transient hygral and thermal analyses are performed to compute the variations over time of relative humidity field $H(t)$ and temperature field $T(t)$. These fields are then imported into an explicit nonlinear FE analysis involving constitutive concrete model, in addition to mechanical loads (hydrostatic and gravity loads). The constitutive model is a mechanical concrete model that uses an orthotropic 3D strain-rotating crack model (Massicotte et al., 2012) and was introduced as a user-subroutine into the software
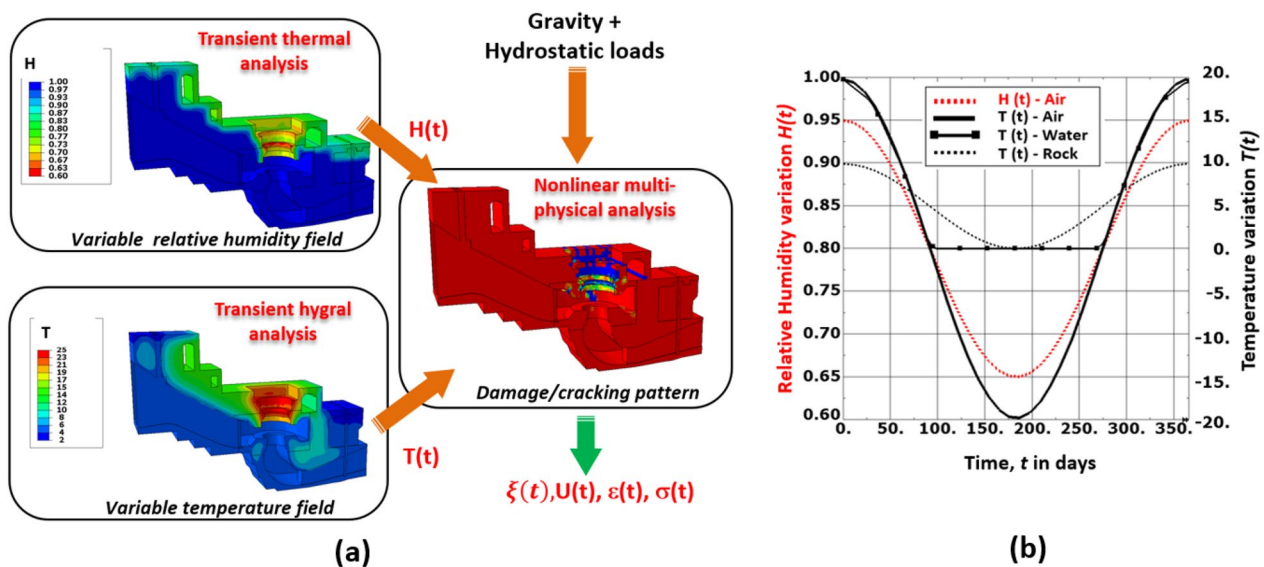
Fig. 5 Computational framework (**a**) and input external conditions for thermal and hygral analyses (**b**)

Abaqus-Explicit (Hibbitt et al., 2017). Over the past years, this mechanical constitutive law has undergone a rigorous verification and validation process (V&V) and was used in the hydraulic structures and bridge engineering industries (Ben Ftima & Massicotte, 2015).

The total incremental strain ($\Delta\epsilon$) is decomposed into mechanical ($\Delta\epsilon_{mec}$), thermal ($\Delta\epsilon_{th}$), creep ($\Delta\epsilon_{cr}$), shrinkage ($\Delta\epsilon_{sh}$) and AAR ($\Delta\epsilon_{aar}$) strain increments according to the following equation in the incremental form:

$$\Delta\epsilon(t, T, H) = \Delta\epsilon_{mec}(t, T, H) + \Delta\epsilon_{th}(t, T)$$
$$+ \Delta\epsilon_{cr}(t, \sigma_0) + \Delta\epsilon_{sh}(t, H) \qquad (2)$$
$$+ \Delta\epsilon_{aar}(t, \xi, T, H, \sigma_0).$$

This equation shows the coupling between the four fields considered in the framework: temperature field T, relative humidity field H, stress field σ_0, and advancement of the chemical AAR reaction field ξ. Both σ_0 and ξ fields are outputs of the final multi-physical explicit analysis (Fig. 5a). The AAR strain increment $\Delta\epsilon_{aar}$ is computed according to Saouma & Perotti, 2006 model (see also Saouma 2015). An example of damage pattern occurring in the semi-spiral case of a powerhouse is shown in Fig. 5a at the year 30 of the AAR pushover analysis. Completely cracked elements are colored in blue, whereas uncracked elements are red-colored. Partially cracked elements (generally at the tips of the cracks) are colored in green. This color convention for the damage pattern is used throughout this paper.

Thermal and hygral analyses were performed in Abaqus-Standard using the implicit solver and transient heat transfer analysis procedure. Thermal analogy was therefore used for the hygral analysis. Fig. 5b shows the imposed external temperature and relative humidity conditions used, respectively, in thermal and hygral analyses. Average daily values are shown for a typical year, and simplified sinusoidal functions are used to represent typical variations of environmental conditions of a typical hydroelectric facility located in northern Quebec. All external temperatures in thermal analysis were applied using convective boundary condition (air temperature for external faces of facility, and water temperature for all wet surfaces including the hydraulic passage). The exception is for the rock temperature which was directly imposed on bottom concrete faces of the facility, as the rock foundation was not included in the transient analysis. Additionally, convective boundary conditions were used for the internal faces of the facility with constant sink temperatures of 15∘C and 25∘C, respectively, for powerhouse interior walls and semi-spiral case turbine pit faces.

Table 1 provides the main input parameters used in the final nonlinear multi-physical explicit analysis. Latency

Table 1 Input data used for the multi-physics analysis

Property	Symbol	Value	Unit
Mass density of concrete	ρ	2400	kg/m³
Young's modulus of concrete	E_c	27,500	MPa
Compressive strength of concrete	f'_c	30.0	MPa
Tensile strength of concrete	f'_t	1.8	MPa
Poisson's ratio of concrete	ν	0.18	–
Mode I fracture energy of concrete	G_F	0.15	kN/m
Yield strength of reinforcement	f_y	400	MPa
Young's modulus of reinforcement	E_s	200,000	MPa
Young's modulus of rock	E_r	50,000	MPa
Poisson's ratio of rock	ν	0.25	–
Long-term volumetric AAR strain	$\varepsilon_{v\infty}$	0.006	–
Reference temperature	T_0	5	°C
Latency time	τ_l	95	Years
Characteristic time	τ_c	13	Years
Activation energy for characteristic time	U_c	5400	°K
Activation energy for latency time	U_L	9400	°K
Compressive limiting stress for AAR	σ_u	10.0	MPa

and characteristic times were chosen to reproduce a typical vertical expansion rate of 20 $\mu\varepsilon$ per year for the assumed monitoring timeframe: from the year 15 to the year 30 assumed to be the present year, as shown in Fig. 3b. Monitoring is therefore assumed to start 15 years after the construction of the facility and this corresponds in the model to the moment when cracking due to AAR becomes visible. The latency and characteristic times are given in Table 1 for a reference temperature of 5 ℃ which is a typical average yearly internal concrete temperature for a typical hydroelectric facility located in northern Canada. The activation energies shown in Table 1 can be used to find the equivalent latency and characteristic times for other temperatures using the Arrhenius law. In a way similar to Saouma 2015, a reduction function $g(H(t)) = H(t)^8$ is used in the computation of AAR strain increment $\Delta\epsilon_{aar}$, to account for the influence of relative humidity. For the mechanical constitutive law, typical values for the input parameters were chosen and correspond to a normal concrete with 30 MPa compressive strength. The long-term asymptotic volumetric strain $\varepsilon_{v\infty}$ provided in Table 1 is another important parameter of AAR kinetics. As schematically shown in Fig. 3b, it controls the asymptotic behavior of the displacement field. A relatively high value has been chosen for this parameter to highlight failure mechanisms in the AAR pushover analysis.

The steel reinforcement was modeled using 1D truss elements embedded in the 3D concrete solid elements (Hibbitt et al., 2017). A simple elastic-perfectly plastic

model was used for steel constitutive model and input parameters are presented in Table 1.

Computation of creep strain is based on the recently developed framework (Ben Ftima et al., 2020), considering a rheological model for creep, accounting for concrete ageing, and based on the generalized Kelvin chain model. As explained in Ben Ftima et al., 2020, identification of Kelvin chain parameters is done according to the CEB-FIP 90 model code by using the compressive strength of concrete as the only required input parameter. By hypothesis, degradation of concrete parameters (compressive/tensile strength, fracture energy and Young's modulus) is not considered in this study. The choice was made to focus on AAR purely structural effects, and thus ignoring degradation effects at the material level. A contact condition with friction (ø = 45°) was assumed between all components of the facility. A condition of full compatibility was chosen between concrete and rock. The external displacement boundary conditions were defined as fixed for the bottom face of the rock and plane strain condition for all the vertical faces of the rock (Fig. 4c). Mechanical loads correspond to self-weight and hydrostatic loads with the assumption of operating condition in all powerhouses (full hydraulic passage) and closed upstream gates of the spillways. Fig. 4d shows in a side view of the facility the applied hydrostatic loads and the upstream/downstream water levels used for the facility. A water density of 1000 kg/m³ was considered. By hypothesis, no uplift pressures in the cracks were considered. The total period of analysis is 100 years. In Fig. 3b,

the year 0 corresponds to the time just after construction and impoundment (i.e., all mechanical loads are already applied). Grouting and slot-cutting repairs were modeled via special programmed user-subroutine in Abaqus-Explicit, VUMAT at the material level (Hibbitt et al., 2017). A linear elastic constitutive model is used. When the input slot-cutting time is reached, the stress transfer is disactivated. This transfer is eventually re-activated, when input grouting time is reached.

3 Assessment of Potential Failure Mechanisms (PFMs)

3.1 Analysis of Displacement Field

Fig. 6 shows the predicted displacement field for the year 50. The *global* tendencies are depicted with black arrows in Fig. 6b. The model shows the tendency of rotation at the left bank corner of the facility due to misalignment of compressive forces coming from the line of the left bank dams and from the line of the powerhouses. The model clearly shows the "squeezing effect" of the spillways between the right-hand side dams and left-hand side powerhouse series. Having clearly less lateral stiffness compared to the other parts, the spillways and more specifically S2 exhibit severe lateral deformations. Finally, the upper part of powerhouse P1 tends to swell towards the downstream/right-side direction which is the local least confined direction.

From a unit *local* point of view, Fig. 6c shows the comparison of deformed/undeformed shapes for the central unit P4. The tilts tendencies of the intake towards
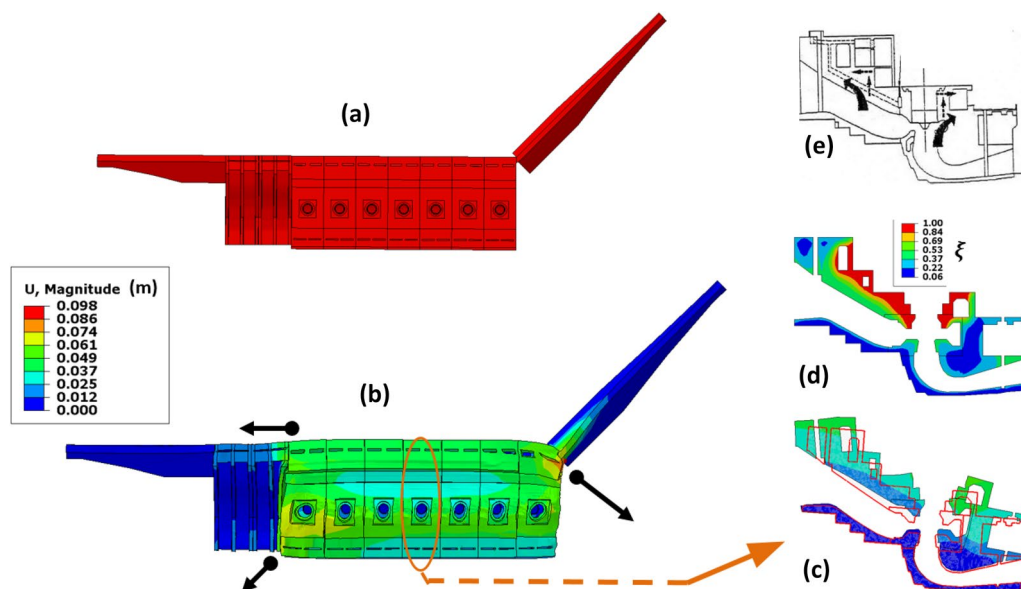
Fig. 6 Analysis of displacement field for the predicted time of 50 years: **a** undeformed shape; **b** deformed shape (× 100); **c** deformed shape of unit P4; **d** advancement of AAR; **e** observed displacements in an existing powerhouse

upstream and semi-spiral case towards downstream are clear in the model and they represent a well observed field tendency in existing similar facilities (Fig. 6e). This can be explained by the AAR advancement field depicted in Fig. 6c, where the AAR advanced more rapidly in the upper part of the semi-spiral case reaching its asymptotic value of 1.0, which means that 100% of the asymptotic volumetric strain is attained. This advancement can be explained by the higher temperatures in this area due to imposed external boundary conditions as explained in "Computational Framework" section (see also Fig. 5 for temperature field). These local and global displacement tendencies will help the interpretation of cracking patterns and expected PFMs considered in the next section.

### 3.2 Cracking Pattern and Potential Failure Modes

Figs. 7 and 8 present the predicted damage (cracking) patterns of the facility. Following the discussion in the previous section, swelling can cause two categories of damage. The first category of *local nature* is related to the stresses induced from restrained swelling at the level of each component of the facility and is depicted in Fig. 7 for the example of the central unit P4. Within this category, the restraint can be internal due to the structural redundancy of the unit or external due to the restraint with rock. The *swelling gradient,* as represented in Fig. 6d, creates also further swelling induced stresses. Fig. 7 shows the evolution of crack patterns with time. It starts with cracking of

the semi-spiral case that appears at the year 15 and ends with a generalized cracking at the year 100. Localized and important cracks evolve along important discontinuities. For example, the inclined shear crack that appeared at year 15 on the wall of the semi-spiral case, propagates along the wall to roof or wall to slab connections and follows the shape of the penstock.

Other cracks initiate and evolve in the stress concentration areas, for example, the slots of the intake gates, around the galleries or at the corners. The first category of cracking can be seen in other units, but as approaching the discontinuities of the facility; here the left-side corner and the P1 to S2 connection on the right side; a second category of cracks shows up and becomes very clear in the components P1, P7 and S2. This second category is of *global nature* and is related to stresses induced by structural discontinuities at the scale of the facility (Fig. 8). Most of these cracks emerge from global displacements that were pointed out with arrows in the previous Fig. 6. One example is the cracking at the top of the intake of P7, but the most important and critical one is the cracking at the interface P1/S2.

From these cracking patterns, it is possible to identify PFMs that may be further considered with a refined local FE model (e.g., substructure) or an advanced engineering phase.

The PFMs are numbered from 1 to 8 and identified using the star symbol in Figs. 7 and 8. They relate either
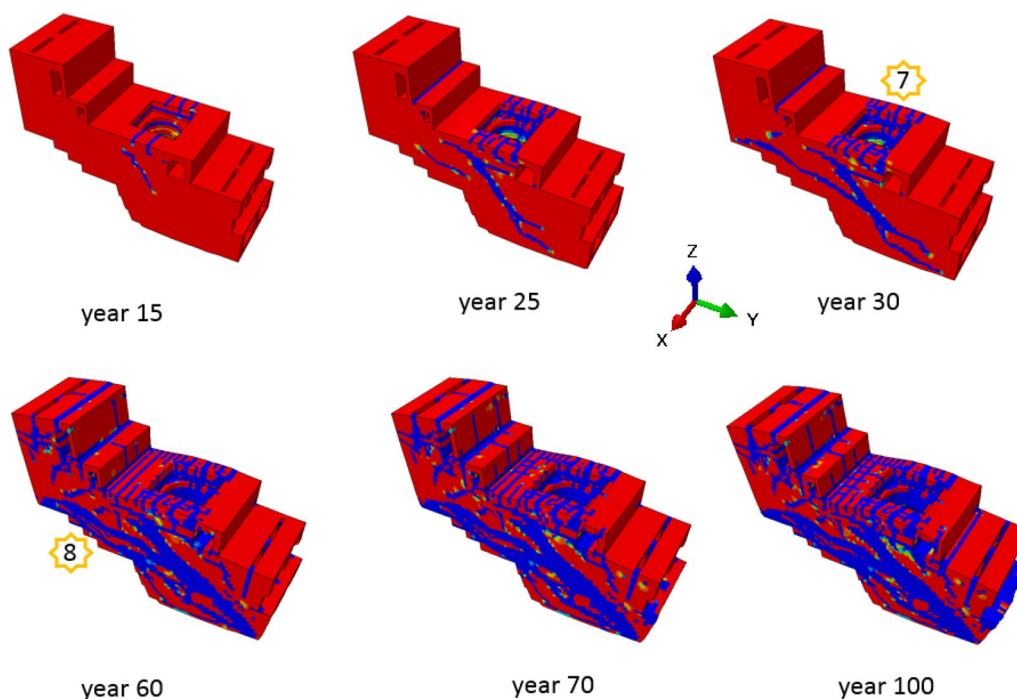
Fig. 7 Predicted local damage pattern for the central unit P4—evolution over time
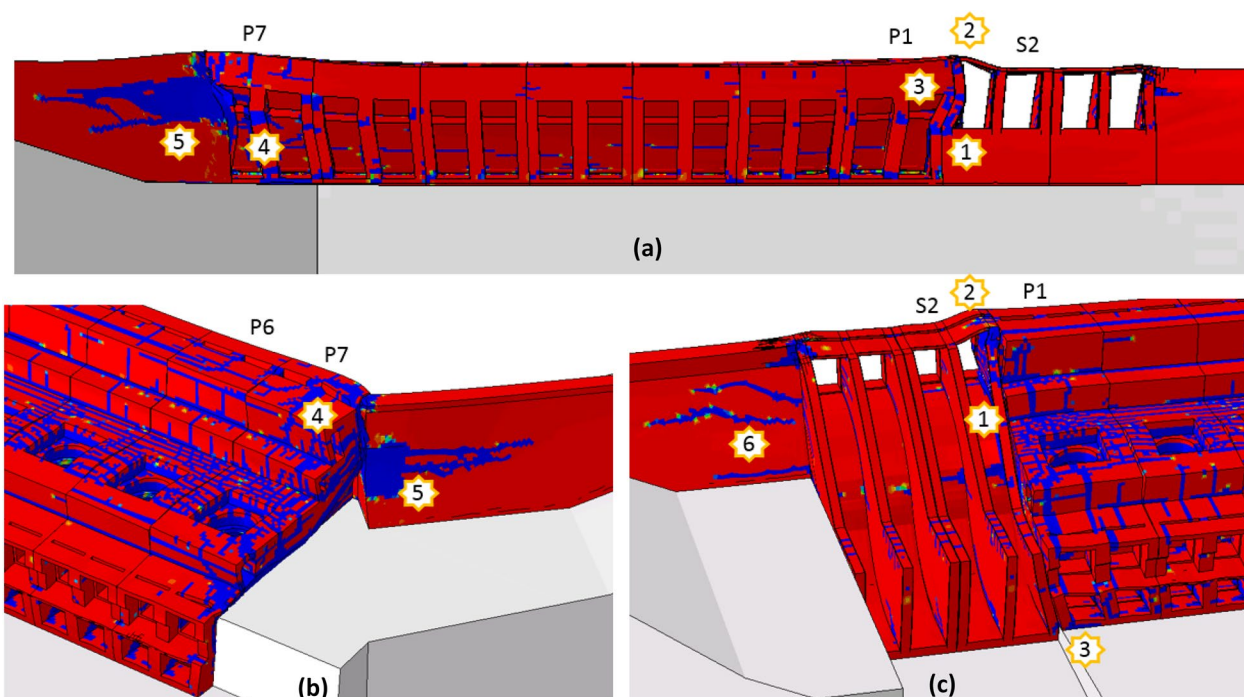
Fig. 8 Predicted global damage pattern for the facility-year 60 (deformation scale × 50): **a** upstream view; **b** downstream left bank view; **c** downstream right bank view

to mass concrete (MC) or to reinforced concrete (RC). The common approach for identifying these mechanisms was the study of crack patterns and its possible interference with stresses induced by force-driven effects (gravity + hydrostatic). AAR effects are driven by deformation but can lead to failure if coupled with effects driven by mechanical loads and while going beyond the ductility limit of an element or a group of elements of the structure (FERC, 2018). The potential failure mechanisms are discussed in the following, mechanism 2 (PFM 2) is detailed in the next section:

(1) Flexural failure or coupled flexural/shear failure of the piers of the spillways under the effect of the thrust from the intake upper blocks. This is a RC failure type which may occur if shear capacity or rotational flexural capacity of the piers are exceeded. Each pier is subjected to bi-axial flexural loading and was originally designed for the uniaxial upstream–downstream flexural effect result of hydrostatic loads acting on the spillway closed gates.

(2) Brittle crushing/splitting failure of the bridge supporting structure above the upstream part of the spillway. This is a RC failure that will be detailed in the next section.

(3) Flexural failure or coupled flexural / shear failure of the right-side wall of P1 (intake + draft tube walls). This is a RC failure type, similar to mechanism (1).

(4) Flexural failure or coupled flexural / shear failure of the left-side wall of P7 (intake only walls, as draft tube walls in this case are supported by rock—Fig. 8b). This is a RC failure type, similar to mechanism (1).

(5) Wedge stability of the upper block of LBGD above the inclined crack. This is a MC failure that can be further studied using 3D stability methods (e.g., Vulliet et al., 2017).

(6) Wedge stability of the block of RBGD above the inclined crack. This is a MC failure, similar to the previous mechanism (5).

(7) Yielding of vertical reinforcement of semi-spiral case walls, due to the formation of horizontal or inclined cracks. This is a RC failure. Vertical reinforcement of semi-spiral case is conventionally designed to resist to the tensile pressurizing effect of the semi-spiral during operation. Due to AAR gradient in the semi-spiral case (Fig. 6d), horizontal

and sub-horizontal cracking occurs in vertical walls (see Fig. 7 year 30) and additional tensile strains arise in the vertical rebars. This PFM can be problematic if deformational yield capacity of the rebars is exceeded.

(8) All other local or global mechanisms that may initiate in planes of weakness induced by critical cracks. A global inclined shear crack becomes visible at year 60 as shown in Fig. 7. It follows the path of the spillway chute. Strength along this weakness plane has to be checked using conventional RC shear friction provisions.

According to authors past experience, crack patterns similar to those in Figs. 7 and 8 have been observed on existing facilities. The identified PFMs are therefore very relevant and shall be considered for existing facilities.

3.3 Local Analysis of Spillway Bridge

A local substructure of the bridge located on top of the hydraulic passage at left side of S2 is considered, as shown in Fig. 9. In the current configuration, the slab is continuous with respect to spillway piers. An additional 15 kPa live load was superimposed to the substructure at the beginning of the analysis (year 0). This additional load was not considered in the global driving model as its effects are assumed negligible on the bridge side faces displacements.

The boundary loads integrated and shown in Fig. 9b at year 30 show a complex multi-axial loading conditions completely different from conventional gravity loading. The acting moments (represented with blue arrows) are

oriented (approximately along Z axis) at an angle close to 90 degrees with respect to gravity induced moments (normally along Y axis). The acting forces (shown in red) have also a nearly compressive orientation. This AAR induced multi-axial loading pattern explains the damage pattern before failure that occurred at year 44.

4 Rehabilitation Strategies and Performance Criteria

4.1 Rehabilitation Strategies

Anchoring, post-tensioning and slot-cutting are conventional local measures used for retrofitting facilities affected by AAR (Fig. 2b). The durability of these *local repair techniques* or the consideration of *global rehabilitation scenarios* are rarely considered in practice due to difficulties mentioned in "Approach Philosophy" section regarding AAR's kinetics (Fig. 2c). Different global rehabilitation scenarios based on slot-cutting are compared in this work. Slot-cutting technique allows reduction of compressive stresses by performing vertical slots (10 to 30 mm in width) using diamond wire saw, at different locations within the facility. Some side effects are, however, related to this technique: (i) this stress release is accompanied by a short-term elastic rebound and a long-term closure of slot walls due to continuation of AAR and delayed effects (Caron et al., 2003; Curtis et al., 2016); and (ii) additional cracking may also occur in the units adjacent to the slot-cut, due to the movement orthogonal to the cutting plane and the increased expansion rate in the direction of tensile stresses, stress concentration at the base of the cut. For these reasons, grouting is considered in this work as a technique that can be combined
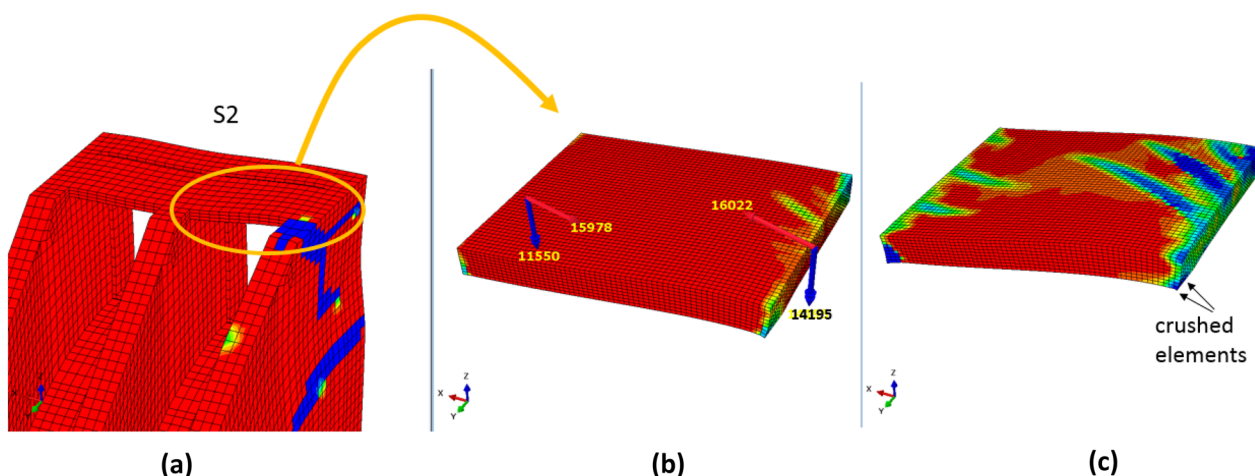
Fig. 9 Local analysis of the spillway's bridge (reinforcement not shown): **a** global model damage pattern at year 30; **b** substructure model damage pattern at year 30 and integrated boundary loads (moments with blue arrows in kN.m, forces with red arrows in kN); **c** substructure model damage pattern before failure at year 44
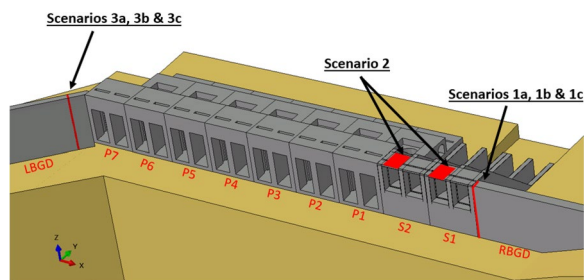
Fig. 10 Rehabilitation scenarios

Table 2 Rehabilitation scenarios

Rehab. scenario	Location	Description
Scenario 1a	RBGD/S1	- Full-depth slot-cut at year 30 - Repetitive re-cuts each 16 years*
Scenario 1b	RBGD/S1	- Half-depth slot-cut at year 30 - Repetitive re-cuts each 16 years*
Scenario 1c	RBGD/S1	- Half-depth slot-cut at year 30 - Grouting of the slot-cut at year 40
Scenario 2	S1 & S2	- Removal of spillway bridge at year 30
Scenario 3a	LBGD/P7	- Full-depth slot-cut at year 30 - Repetitive re-cuts each 11 years*
Scenario 3b	LBGD/P7	- Half-depth slot-cut at year 30 - Repetitive re-cuts each 11 years*
Scenario 3c	LBGD/P7	- Half-depth slot-cut at year 30 - Grouting of the slot-cut at year 40

* Frequency of the re-cuts assessed using FE models assuming a 25-mm cut

with slot-cutting in a given scenario to minimize stress release and excessive movements effects.

Analysis of the damage/cracking pattern of the facility conducted in previous section showed two categories of damage: local and global. Slot-cutting is believed to be more efficient when targeting the global category of damage, due to the global effect of the discontinuities. For this reason, all considered rehabilitation scenarios in this study are selected in the neighborhood of the discontinuities identified for this facility. In total, seven scenarios are considered (Fig. 10; Table 2). For each scenario, an AAR pushover nonlinear multi-physics analysis was performed using the same inputs and methodology described in "Computational Framework" section.

Scenarios 1a and 3a consider full-depth slot cuts, whereas 1b and 3b consider half-depth slot cuts. For these four scenarios, repetitive re-cuts are required to maintain the opening of the slot walls. Frequencies of the re-cuts shown in Table 2 were estimated using initial closure rates from FE analyses. Due to the non-linearity of the swelling curve (Fig. 2c), these closure rates can double over time, thus increasing the frequency of the re-cuts.

In scenarios 1c and 3c, grouting is performed into the cut, ten years after the initial slot-cut. In scenario 2, the longitudinal support brought by the spillway bridge disappeared by removing the bridge. This remedial measure may be required before concrete crushing.

4.2 Performance Criteria

Standard performance criteria developed in the literature were generally based on the displacement field output of the FE analyses (whether linear or nonlinear). The spillway gate closure and the lateral spillway pier displacement are examples of local metrics that can be used for this purpose. These metrics do not allow to fully benefit from the results of advanced nonlinear analyses which additionally allow to capture cracking of the facility and identify potential failure mechanisms. The damage pattern from smeared cracking models when using an adequate refined mesh (e.g., Figs. 7, 8 and 9), provides an interesting information regarding the cracking pattern. However, this metric is still qualitative. A new metric is suggested in this study for this purpose, inspired from the cracking index diagnosis method used in industry (ISE, 1992; LCPC, 1997). The original cracking index method consists in the measurement and summation of crack widths along a set of lines drawn perpendicularly on the surface of the concrete element investigated and gives a local assessment of the extent of cracking. This method is known to have some limitations when used with AAR: local assessment of damage and not global, surface and not volumetric cracking, contamination with other surface effects such as freeze and thaw cycles, shrinkage and temperature gradients. Rather than considering a surface cracking, the metric considered in this study, called *TCW* (for total crack width) considers all the volumetric cracking caused by AAR within all elements of a given volume V:

$$TCW(t, V) = \int_0^t \left(\sum_V \left(\frac{v_e}{\bar{v}} . h_e . \Delta\varepsilon_{cr-max} \right) \right) dt, \quad (3)$$

where V is the total volume considered (e.g., a unit of the facility or a component of unit); v_e is the volume of a given mesh element of that volume, h_e is characteristic length of the element; $\bar{v}$ is the average volumetric element for all elements in V. For FE model with relatively uniform mesh size, $\frac{v_e}{\bar{v}} \approx 1.0$, $\Delta\varepsilon_{cr-max}$ is the principal cracking strain increment occurring in the element, within increment dt.
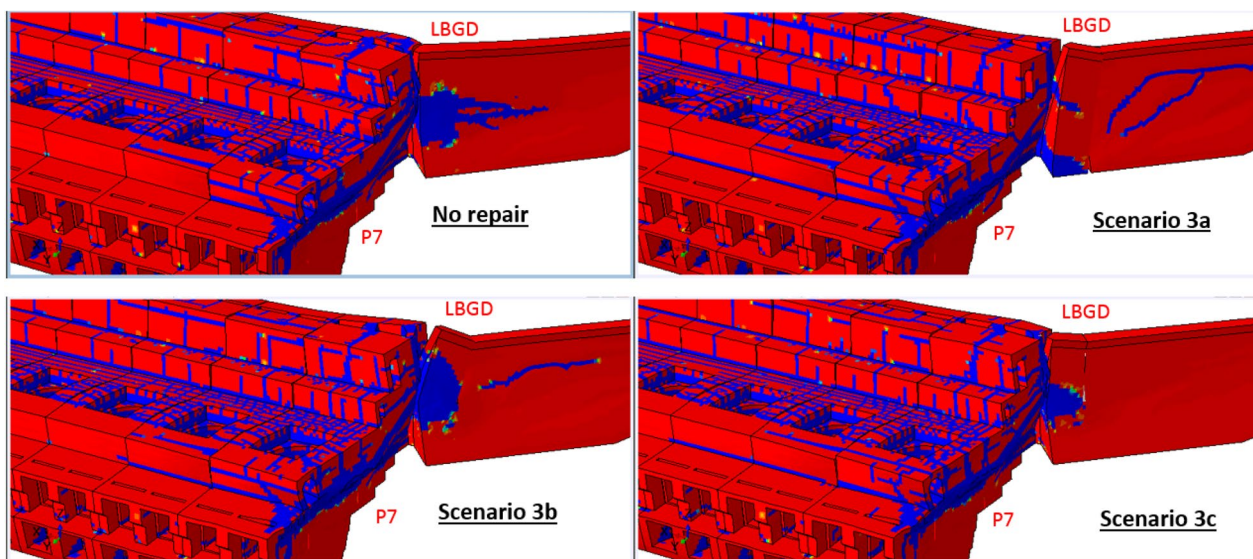
Hence, *TCW* represents qualitatively the summation of the crack widths over the elements of volume V and is expressed in units of length (e.g., in mm). It can be computed for each unit of the facility at a given time.
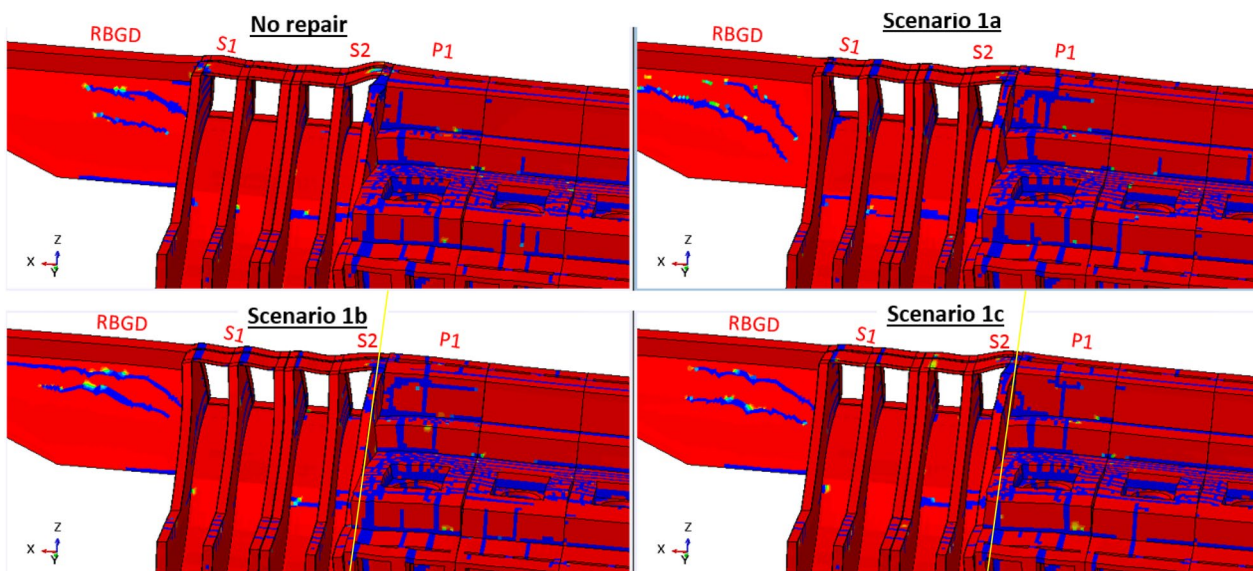
Fig. 11 Cracking pattern for scenarios 1—slot-cut at RBGD/S1 (t = 60 years, def. scale × 50)
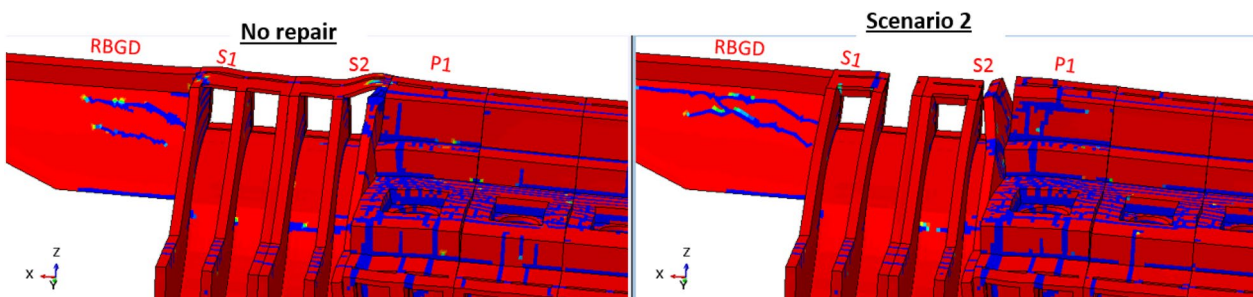
Fig. 12 Cracking pattern for scenario 2—removal of bridge (t = 60 years, def. scale × 50)

Fig. 13 Cracking pattern for scenarios 3—slot-cut at RBGD/S1 (t = 60 years, def. scale × 50)

It can also be computed for a particular component of interest within the facility (e.g., spiral cases of all units) or even computed for the overall facility.

5 Results and Discussion

5.1 Cracking Pattern and TCW

Figs. 11, 12, 13 present the comparative cracking patterns between the scenarios at the year 60, so 30 years after the initial intervention. The depth of the slot-cut in either scenarios 1 or 3 clearly influences the orientation of the cracks in the adjacent dam (RBGD for scenarios 1, and LBGD for scenarios 3). This understandable phenomenon is linked to the vertical position of the starting position of the compressive forces, located just below the cut. Scenario 1c when compared to 1a, 1b and 2 seems to give the least amount of damage to units S2 and P2. On the other side, Scenario 2 is the worst from this point of view, and the excessive lateral deflection of S2 can be clearly noticed from Fig. 12. According to Figs. 12 and 13, all the rehabilitation scenarios appear to result in more cracking if compared to the case without rehabilitation.

Scenario 3b if compared to scenarios 3a and 3c (Fig. 13) results into more local damage. Examination of FE results

actually shows a local failure at the left-side intake pier of unit P7 due to location of slot-cut at the mid-depth of LBGD.

Comparison of scenarios using visual inspection of cracking pattern is not usually simple. The use of a quantitative metric such as TCW is therefore recommended. Fig. 14 shows the computed values of TCW for all the components of the facility, at years 60 and 90. The first interesting thing to note is the two-peak distribution of all curves. The two peaks are located around the two discontinuities S2/P1 and P7/LBGD. When comparing TCW values for the case without rehabilitation for units P7 and P1 with respect to central unit P4, global damage category contributes to 25% to 70% more damage if compared to the local damage category.

The effects of a scenario may be beneficial for one component but not beneficial for other components. For example, scenarios 3a, 3b and 3c resulted in less cracking in the LBGD with comparison to the case without rehabilitation, whereas they produced more cracking in the unit P7 and P6. Table 3 gives the best two scenarios for each component of the facility for the years 60 and 90. It appears from this table that classification does not
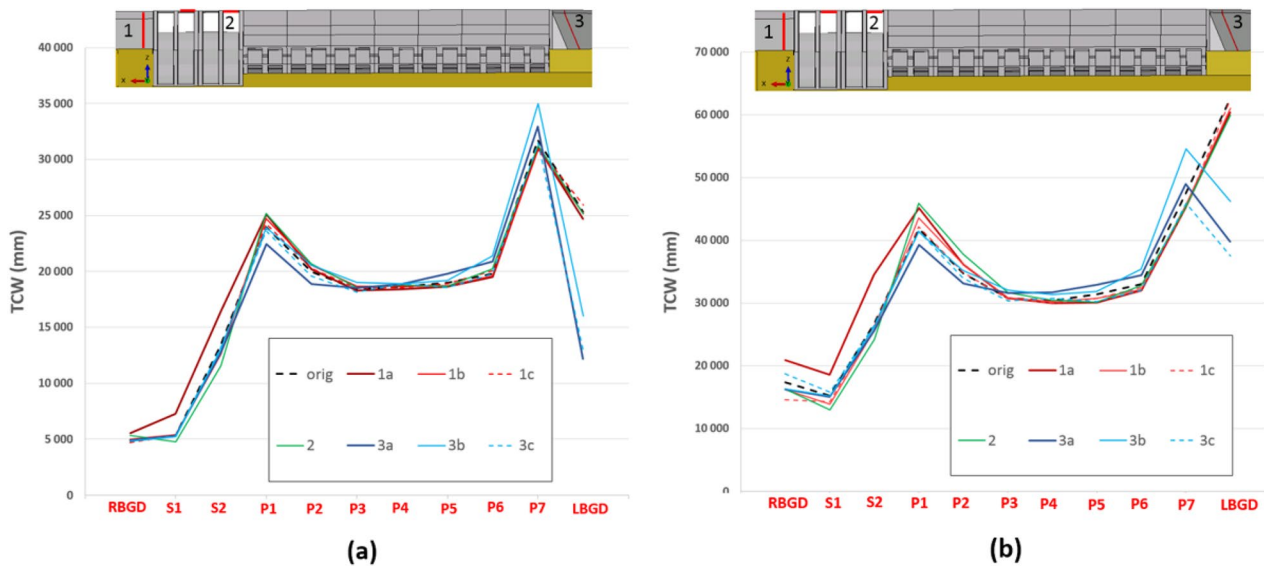

Fig. 14 Assessment of TCW: **a** t = 60 years; **b** t = 90 years

**Table 3** Best scenarios in terms of cracking (TCW)

Unit	RBGD	S1	S2	P1	P2	P3	P4	P5	P6	P6	LBGD
Best scenarios (t = 60 years)	1c, 3b	2, 3b	2, 1b	3a, 3c	3a, 3c	3c, 3b	1a, 1c	3c, 1a	1a, 1b	1b, 1c	3a, 3c
Best scenarios (t = 90 years)	1c, 1b	2, 1b	2, 3a	3a, 3b	3a, 3c	3c, 1c	1a, 1c	1a, 2	1a, 1b	1a, 1b	3c, 3a

change much with time. By considering all the facility, the best scenarios with respect to the global TCW metric are 3c, 3a and 1c with TCW reductions of 8%, 7% and 2% with respect to the case without rehabilitation. Scenario 1a was the worst and resulted in an increase of 4% of the global TCW with respect to the case without rehabilitation. As it will be explained in the next section, this result is linked to a local failure occurring in spillway S1.

5.2 Displacement Metrics

Fig. 15a presents the evolution over time of the spillway S1 gate closure. The closure limit of 25 mm is considered for gate jamming. Due to repetitive re-cuts, jamming is prevented using scenarios 1a and 1b. The same result was also obtained with scenario 2. Repetitive slot-cutting

at mid-depth (using scenario 1b) was enough to prevent jamming. Unlike all other rehabilitations, an opening was recorded for scenario 1a (complete cut). This can be explained by Fig. 15b presenting the cracking pattern at year 90. Cutting at full depth resulted in inclined shear cracking at the base of S1, and more specifically under the right-side pier. This adverse effect resulted in an excessive lateral displacement of the right-side pier for scenario 1b. Comparing cracking patterns in Fig. 15b clearly shows the advantage of slot-cutting at mid-depth for this location. Interestingly, jamming is delayed by about 25 years using scenario 1c, with respect to the case without rehabilitation. Also, and as anticipated, scenarios 3a, 3b and 3c had little effects with respect to this performance criteria.
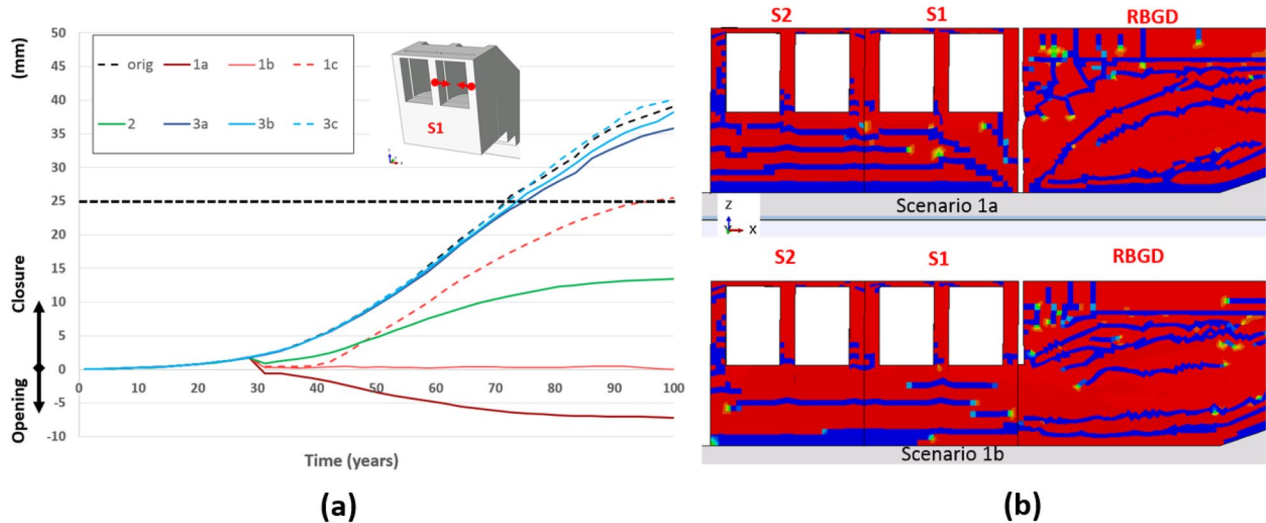
Fig. 15 Gate closure: **a** evolution over time; **b** cracking pattern (t = 90 years)

Table 4 Summary comparison table of performance metrics

Performance metric	Advantages	Disadvantages
Displacement field	- Can be used even with linear fe analyses - Simple to use and interpret - Quantitative	- Does not provide a pertinent information on the crack extent and potential failure mechanisms
Damage pattern	- Can be used to detect potential failure mechanisms - Suitable for nonlinear fe analyses	- Nonlinear FE expertise required - Expert engineering judgement is required to detect potential failure mechanisms - A well refined mesh and a validated constitutive model are required
New suggested TCW metric	- Suitable for nonlinear fe analyses - Quantitative - Can be used at local or global scale of facility	- Nonlinear FE expertise required - Can give information on potential failure mechanisms but expert judgement is still required

6 Discussion

When considering all performance criteria, and the compromise between stress relief/cracking extent, a combination involving both scenarios 1c (partial cut + grout) and 3c (partial cut + grout) appears to be an interesting starting solution for this representative facility. Scenario 3c offers the advantage of a generalized stress relief whereas scenario 1c offers the best solution for the spillway gate jamming problem. According to this study, grouting technique can be beneficial when combined with slot-cutting. The choice of grouting time and location can further be optimized to allow enough stress release, while restoring the beneficial confinement and load transfers.

To conclude this section, and based on the comparative work conducted by authors in this study, a summary Table 4 is provided to compare the different performance metrics that can be used to assess different retrofitting strategies, in the field of concrete facilities affected by AAR. Of course, cost-effectiveness and operational related metrics are excluded from this table as they are outside the scope of this work.

7 Suggested V&V Benchmarks

According to the philosophy of this work, the development of pertinent V&V benchmark problems (BP) is one of the outcomes of the AAR pushover approach. Following the top-down approach as described in Fig. 3.a, three developed BPs are presented in this section. According to results of "Assessment of Potential Failure Mechanisms (PFMs)" section, PFM 2, related to spillway bridge deck failure was one of the most critical failure mechanisms due to its brittle nature. Along the X direction of the facility, the bridge deck can be viewed as small structural element subjected to compressive stresses from adjacent stiff elements (see Fig. 10). The structural system can be considered as a series system where the brittle failure of one member (in this case, the weakest member is

the bridge deck) leads to immediate failure of the entire system.

BP1, BP 2 and BP 3 as shown in Fig. 16 were therefore designed to represent configurations where a series system of two elements is subjected to a restrained swelling along a principal direction. The small element (representative of bridge deck) is adjacent to relatively larger and stiffer element (representative of dam crest). No AAR gel expansion can occur at stress intensity above 8 to 10 MPa. This compressive limiting stress for AAR kinetics is generally a material input parameter in multi-physic models (parameter $\sigma_u = 10$ MPa in Table 1; Fig. 17) (Léger et al., 1996; Saouma, 2014). Therefore, theoretically no failure can occur when a single prismatic concrete element is subjected to self-restrained swelling. This case is represented by configuration BP 1 in Fig. 16, where the restrained swelling direction is along X axis. However, when two adjacent elements with different cross sections are subjected to restrained swelling, the behavior completely changes. Compressive stresses in the smaller element (e.g., bridge deck) can exceed the AAR limiting stress because they are controlled by swelling of the larger element (e.g., dam). Furthermore, the stress distribution is no more uniform near the junction of the two elements. Tensile stresses can develop in the perpendicular direction to the principal compressive stresses (similar to local post-tension effects) leading to splitting failure. These situations are represented by configurations BP 2 and BP 3. The only difference between these two configurations is the steel reinforcement added for BP 3 to control the tensile stresses near the junction, on the side of the larger element.

Fig. 17 presents the simulation results tentatively performed using the constitutive modeling described previously and the same input data in Table 1, except for the compressive stress ($f'_c = 40MPa$). In Fig. 17b, the compressive stresses along the X axis are averaged for the last
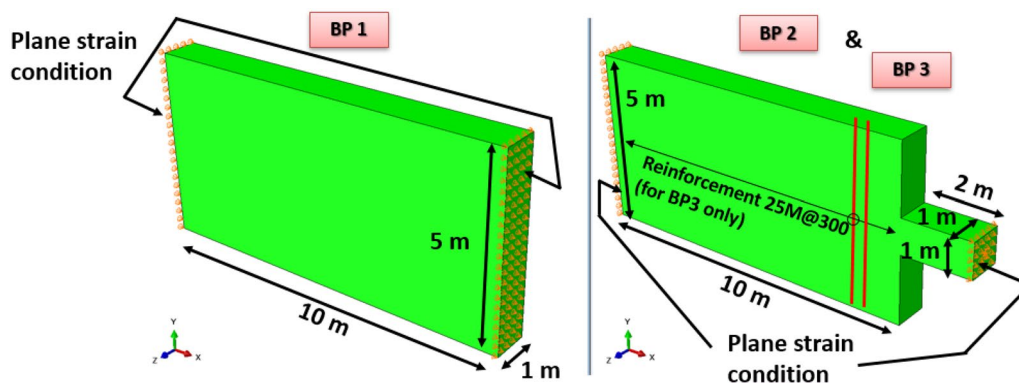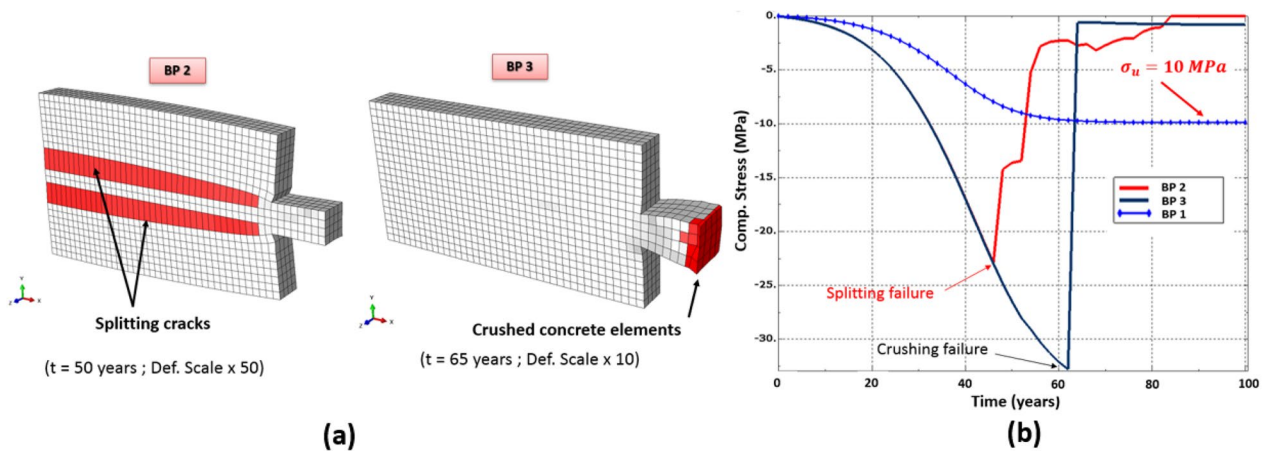

Fig. 16 Description of numerical benchmark problems based on PFM 2

Fig. 17 BP results: **a** failure modes, **b** results of transferred compressive stress vs time

row of concrete elements subjected to plane strain condition. While no failure was recorded for BP1, splitting and crushing failures occurred, respectively, for BP 2 and BP 3 at years 50 and 65. As expected, the compressive stresses in BP 1 capped at a value of $\sigma_u = 10$ MPa, which is much smaller than the compressive strength of the concrete (40 MPa), and no compressive crushing occurred. Tensile stresses developed in BP 2 along Y direction, and because no reinforcement is provided, splitting cracks propagated along X direction, causing failure. The presence of rebars in BP 3 allowed to control concrete cracking after its initiation. Crushing failure occurred at year 65 when the compressive stresses reached the compressive strength of concrete.

8 Conclusions

This work presented a study of potential failure mechanisms and comparison of rehabilitation scenarios for typical hydroelectric facilities affected by AAR. An innovative approach was followed by performing an AAR pushover analysis using chemo-mechanical advanced simulation on a representative hydroelectric facility.

The following conclusions can be drawn, following this study:

– Even if AAR effects are driven by deformations, they may become structurally critical to some concrete or reinforced concrete elements of the facility, when superimposed to load-driven effects such as hydrostatic loads.
– By analyzing displacement field and cracking of the facility, two different categories of damage were detected: local and global damages. The global damages originate from stiffness and geometrical discon-

tinuities at the level of facility and are the most critical in terms of the failure mechanisms.
– Rather than using the numerical methods solely as continuous structural health monitoring tools calibrated with monitoring data, the AAR innovative pushover approach allowed to capture the potential failure mechanisms and assess the performances of different rehabilitation scenarios. Using this approach, an educated decision could be made for planning timely interventions: a key requirement for the management of the facility and continuous production of electricity.
– Potential failure mechanisms can be used, as shown in this work for the example of bridge deck failure, to develop pertinent benchmark numerical problems for verification and validation purposes of AAR constitutive models. Contrarily to the conventional bottom-up approach, the followed top-down approach allowed to develop benchmarks at higher levels than the conventional material and element levels.
– Using performance metrics and newly developed metric suitable for nonlinear FE analyses, it was possible to compare different global rehabilitation scenarios. The combination of the grouting technique with the conventional slot-cutting technique (scenarios 3c and 1c) resulted in the best compromise in terms of stress relief and extent of cracking.
– Although clearly much work remains to be done for the sophisticated models for the prediction purpose of long-term behavior, they can be however used as demonstrated in this work, as an interesting tool within an overall progressive assessment methodology. Important outcomes are expected from the

results of sophisticated FE analyses and can feed advanced engineering phases.

Authors' information
Mahdi Ben Ftima: Associate Professor, P.Eng., Ph.D., Department CGM (Civil, Geological and Mining Engineering), Polytechnique Montréal, P.O. box 6079, station Centre-ville, Montréal, Québec, H3C 3A7, Canada. Emre Yildiz: President, P.Eng., M.Eng., PMP, IDAE, Montréal, Québec ,H2Y 1W8, Canada.

Availability of data and materials
The numerical model of the facility can be provided through request to authors under certain conditions for publication.

Declarations

Competing interests
The authors wish to confirm that there are no known conflicts of interest associated with this publication and there has been no significant financial support for this work that could have influenced its outcome.

References
Caron, P., Léger, P., Tinawi, R., & Veilleux, M. (2003). Slot cutting of concrete dams: Field observations and complementary experimental studies. *ACI Structural Journal, 100*(4), 430–439.

Comi, C., Fedele, R., & Perego, U. (2009). A chemo-thermo-damage model for the analysis of concrete dams affected by alkali-silica reaction. *Mechanics of Materials, 41*, 210–230.

Curtis, D.D, Feng, L., Sooch, G.S, & Zheng, F. J. (2016). Practical analysis and assessment of AAR-affected dams and hydroelectric plants. *36th annual USSD conference*, Denver, USA.

FERC (2018). Engineering guidelines for the evaluation of hydropower projects Chapter 11—arch dams, Federal Energy Regulatory Commission, Washington, DC, USA.

Ftima, M. B., Joder, M., & Yildiz, E. (2020). "Creep modelling for multi-physical simulation of mass concrete structures using the explicit finite element approach. *Engineering Structures, 212*, 110538.

Ftima, M. B., Léger, P., & Boussaha, F. (2017). "Nonlinear finite elements for the assessment of hydraulic concrete structures affected by alkali-aggregate reaction: a case study." *Dam Swelling Concrete (DSC 2017)*, Chambéry, France.

Ftima, M. B., & Massicotte, B. (2015). Utilization of nonlinear finite elements for the design and assessment of large concrete structures. Part I: Calibration and Validation. *ASCE Journal of Structural Engineering, 141*(9), 04014218.

Gocevski, V., & Yildiz, E. (2017). Macro-Modelling of AAR-affected hydraulic structures-Assessment of parameters influencing the in-situ concrete growth. *Dam Swelling Concrete (DSC 2017)*, Chambéry, France.

Hibbitt, H. D., Karlson, B.I., & Sorensen, E. P. (2017). ABAQUS version 2017, finite element program, Hibbitt, Karlson and Sorensen, Providence, R.I.

ISE. (1992). Structural effects of Alkali-Silica reaction: Technical guidance on the appraisal of existing structures. Institution of Structural Engineers (ISE), London. UK, 1992.

Larive, C. (1998). Apports combinés de l'expérimentation et de la modélisation à la compréhension de l'Alcali-Réaction et de ses effets mécaniques. Thesis (in French), LCPC, Paris.

LCPC. (1997). Determination de l'indice de fissuration d'un parement de beton. Méthode d'essai LCP. vol. 47, Laboratoire central des ponts et chausses (PCPC). Paris. France.

Léger, P., Côte, P., & Tinawi, R. (1996). Finite element analysis of concrete swelling due to alkali-aggregate reactions in dams. *Computers and Structures, 60*, 601–611.

Léger, P., Tinawi, R., & Mounzer, N. (1995). Numerical simulation of concrete expansion in concrete dams affected by alkali-aggregate reaction: State-of-the-art. *Canadian Journal of Civil Engineering, 22*, 692–713.

Massicotte, B., Nour, A., Ben Ftima, M., Yildiz, E., & Conciatori, D. (2012). *EPM3D v2.0, A user-supplied constitutive model for the nonlinear finite element analysis of concrete structures.* Research report, École Polytechnique de Montréal.

Oberkampf, W. L., & Roy, C. J. (2010). *Verification and validation in scientific computing.* Cambridge University Press.

Omikrine, M. O., Seignol, J.-F., Rigobert, S., & Toutlemonde, F. (2014). Modelling the cracks opening-closing and possible remedial sawing operation of AAR-affected dams. *Engineering Failure Analysis, 36*, 199–214.

RILEM State-of-the-art-report, TC259-ISR. (2019). *Diagnosis and prognosis of AAR affected structures—final draft version.",* Victor Saouma Editor, Technical Committee 259-ISR.

Saouma, V., & Perotti, L. (2006). Constitutive model for alkali aggregate reactions. *ACI Materials Journal, 103*(3), 194–202.

Saouma, V. E. (2014). *Numerical Modeling of AAR.* CRC Press Taylor & Francis Group.

Sellier, A., Bourdarot, E., Multon, S., Cyr, M., & Grimal, E. (2009). Combination of structural monitoring and laboratory tests for assessment of alkali-aggregate reaction swelling: Application to gate structure dam. *ACI Material Journal, 106*, 281–290.

USBR (2005). Effects of concrete deterioration on safety of dams, Report No. DSO-03-05, Department of the Interior, Bureau of Reclamation, Technical Service Center Denver, Colorado.

Vulliet, F., Ben Ftima, M., & Léger, P. (2017). Stability of cracked concrete hydraulic structures by nonlinear quasi-static explicit finite element and 3D limit equilibrium methods. *Computers and Structures, 184*, 25–35.

Publisher's Note
Springer Nature remains neutral with regard to jurisdictional claims in published maps and institutional affiliations.